

GLOBAL RECOVERY FROM LOCAL DATA: INTERIOR NUDGING FOR 2D NAVIER-STOKES EQUATIONS IN A PHYSICAL DOMAIN

RUI FANG AND ALI PAKZAD*

ABSTRACT. In many real-world applications of data assimilation (DA), the strategic placement of observers is crucial for effective and efficient forecasting. Motivated by practical constraints in sensor deployment, we show that global recovery of the flow field can be achieved using observations available only in a subregion of the domain, possibly far from the boundary. We focus on the two-dimensional incompressible Navier–Stokes equations posed in a bounded physical domain with Dirichlet boundary conditions. Building on the continuous data assimilation framework of Azouani, Olson, and Titi (2014), we rigorously prove that the assimilated solution converges globally to the true solution under suitable conditions on the nudging parameter, spatial resolution, and the geometry of the observation region, specifically, when the maximum distance from any point in the domain to the observational subregion is bounded by a constant multiple of $\nu^{1/2}$ (in terms of scaling). Our computational results, conducted via finite element methods over complex geometries, support the theoretical findings and reveal even greater robustness in practice. Specifically, synchronization with the true solution is achieved even when the observational subregion lies farther from the rest of the domain than the theoretical threshold permits. Across all three tested scenarios, the local nudging algorithm performs comparably to full-domain assimilation, reaching global accuracy up to machine precision. Interestingly, observational data near the boundary are found to be largely uninformative. This demonstrates that full observability is not necessary: carefully chosen interior observations, even far from the boundary, can suffice.

1. INTRODUCTION

Data Assimilation (DA) refers to a class of methodologies that combine observational data with mathematical models to improve the accuracy of forecasts [2, 46]. As the volume and quality of observational data grow rapidly, thanks to advances in sensing technologies and computational power, the role and impact of DA techniques have become increasingly vital for scientific prediction. In weather and turbulence forecasting, observations are collected by instruments such as weather stations, sensors, or ocean buoys, all of which require significant

2010 *Mathematics Subject Classification.* Primary: 35Q30, 34D06. Secondary: 35Q93, 93B07, 76D10.

Key words and phrases. Data assimilation, Navier-Stokes Equations, Turbulence, Sensor Placement, Prandtl boundary layer.

*Corresponding author. Email: pakzad@csun.edu.

manpower, financial resources, and logistical planning. Optimal placement of these observers is a central challenge in the design, prediction, estimation, and control of high-dimensional systems (such as weather prediction models) [14]. For example, it is much easier to measure fluid velocity or temperature at shallow ocean depths than at extreme depths. Likewise, deploying a dense array of uniformly placed sensors is plainly infeasible in settings like modeling the solar wind. Therefore, from a practical standpoint, sensor placement strategies must account for resource limitations while still achieving high prediction accuracy. By identifying where data are most informative, we can reduce the number of sensors needed while improving model performance. There has been tremendous effort in recent years within the fields of control theory and inverse problems to provide guidance on optimal sensor placement for improved flow prediction [5, 10, 19, 56, 58, 59]. In fact, it is well understood that not all observation locations contribute equally to state estimation [14, 59]. Despite this, with the notable exception of the work by Biswas, Bradshaw, and Jolly [6], the majority of existing rigorous and computational results in the direction of Continuous Data Assimilation [3] (CDA; see Subsection 1.1) assume *global observability*; that is, observational data are assumed to be uniformly available throughout the entire spatial domain. This assumption, while mathematically convenient, poses serious limitations for real-world applications. Our work challenges this framework by showing that it is possible to recover the full system dynamics using only local observational data from a subregion of the domain.

In this paper, we conduct a rigorous analysis, accompanied by a comprehensive computational study, of a **global DA algorithm that relies solely on local observations**. Our focus is on the two-dimensional Navier-Stokes equations (NSE) posed in a bounded physical domain Ω , subject to Dirichlet boundary conditions

$$(1.1) \quad \partial_t \mathbf{u} + (\mathbf{u} \cdot \nabla) \mathbf{u} - \nu \Delta \mathbf{u} + \nabla p = \mathbf{f}, \quad \nabla \cdot \mathbf{u} = 0, \quad \text{in } \Omega \times (0, \infty),$$

with the initial condition $\mathbf{u}_0 = \mathbf{u}(x, 0)$, which is typically not fully known in practice. Here, $\mathbf{u} = \mathbf{u}(x, t)$ denotes the “true” velocity field, $p = p(x, t)$ is the pressure, $\mathbf{f} = \mathbf{f}(x, t)$ is a given external body force, and $\nu > 0$ is the kinematic viscosity. When using the NSE, or any other relevant nonlinear model, for weather prediction, the exact initial condition \mathbf{u}_0 is typically not fully known a priori [43]. This uncertainty in the initial data can lead to significant challenges, as even small errors may grow exponentially in time due to the nonlinear nature of the system [43, 48–50]. To overcome this difficulty, in DA, the observational measurements are directly inserted into a mathematical model [35, 44].

Motivated by [3], we now introduce the framework of *local DA*, where the solution \mathbf{u} is only partially and locally known, specifically in a subregion located *far* from the boundary. Specifically, we assume that coarse spatial observations of the velocity field are available *only* within an interior subdomain $\Omega_0 \subset \Omega$ (see Figure 1a), and not throughout the entire physical

domain Ω . These observations are represented by an interpolation operator $I_H(\mathbf{u})$, which acts on \mathbf{u} to extract its values on a coarse spatial grid of resolution H supported in Ω_0 . The corresponding local DA algorithm is formulated as the following modified Navier–Stokes system with the same Dirichlet boundary conditions in the physical domain Ω

$$(1.2) \quad \partial_t \mathbf{v} + (\mathbf{v} \cdot \nabla) \mathbf{v} - \nu \Delta \mathbf{v} + \nabla q = \mathbf{f} + \mu(I_H(\mathbf{u}) - I_H(\mathbf{v})), \quad \nabla \cdot \mathbf{v} = 0, \quad \text{in } \Omega \times (0, \infty),$$

where

I_H : localization operator that incorporates observational data only from a designated subregion Ω_0 of the domain,

and the initial value of $\mathbf{v}(x, 0) = \mathbf{v}_0$ is arbitrary. Here, $\mathbf{v} = \mathbf{v}(x, t)$ is the “approximate” velocity field, and $\mu > 0$ is a relaxation (nudging) parameter.

Results in this paper. Having established the framework in (1.2), we provide a rigorous analysis showing that it is possible to recover the full flow field using velocity observations collected only from an interior portion of the domain, without requiring measurements near the boundaries. Specifically, we prove in Theorem 4.1 that if no part of the domain lies too far from the observational subregion (more precisely, if the maximum distance from any point in the domain to the observation region remains below a fixed threshold proportional to the square root of viscosity in terms of scaling, $\delta \lesssim \nu^{1/2}$ ¹) then, under standard conditions on the nudging parameter and spatial resolution, the locally assimilated solution (1.2) converges globally to the true solution of the 2D NSE(1.1). This result demonstrates that achieving global accuracy does not require global data, and quite surprisingly, not even data near the boundary. However, carefully chosen, localized observations from the interior of the domain can be sufficient.

We demonstrate the efficacy of the algorithm through extensive computational studies. In all experiments, we implement the finite element method for simulations over complex geometries with irregular domains and realistic boundary conditions. A key technical challenge, and novelty, of this work lies in constructing a local, coarse finite element mesh for the interpolation operator that is compatible with the global fine mesh used to solve the full system. This compatibility ensures mathematical consistency and numerical stability while enabling localized DA. Three flow scenarios are tested

- (1) Flow over a flat obstacle (see Section 5),
- (2) Couette/Shear flow in an annulus (see Section 6),
- (3) Flow driven by a body force in a disk with an off-center obstacle (see Section 7).

¹This is the same scaling that governs the thickness of the classical Prandtl boundary layer[53], suggesting a potential connection between the effectiveness of interior observations and the physical structure of near-wall viscous flow.

All flows are simulated within a bounded physical domain under Dirichlet boundary conditions. All three simulations are in agreement with the theoretical results proved in Theorem 4.1. We observe that the local nudging algorithm achieves global synchronization within machine precision, typically at a slightly (but not significantly) slower rate compared to full-domain nudging, when the data are collected from an interior subregion far from the boundaries. In nearly all simulations, observational data near the boundaries are found to be uninformative for the nudging algorithm. To ensure that this effect was not simply due to variations in data density or the number of observational points, we also varied the area of the local DA region. Nevertheless, the same trend was consistently observed: interior observations led to effective synchronization, while boundary observations remained largely uninformative.

The theoretical strict conditions on the parameters, namely the nudging parameter μ , the density of observational points H , and the distance δ between the observational subregion and the rest of the domain, can be significantly relaxed in practice. Even when the local observation region lies farther from the boundaries than the theoretical threshold permits, the local assimilation algorithm still performs well, achieving global synchronization with the true solution up to machine precision. This theoretical restrictions is well accepted in the frame work of the data assimilation (see, for instance, [11, 12, 22, 30, 32, 39, 54, 61]).

1.1. Global Continuous Data Assimilation. Using observational data to improve the predictive capability of mathematical models dates back to the work of Rudolph Kalman in 1960 [42], and of Charney, Halem, and Jastrow in 1969 [13], following the advent of satellite-borne observation systems that began producing climate data. In the same direction, DA aims to recover the fine-scale dynamics of a system using only coarse, partial observations [16, 43]. A notable contribution in this area is the work of Azouani, Olson, and Titi [3], who introduced a nudging-based DA algorithm (a.k.a. CDA) that is mathematically rooted in earlier work of Foias and Prodi [25] on determining functionals. One of the key advantages of their approach lies in its simplicity of implementation and its compatibility with rigorous mathematical analysis, making it a compelling alternative to other data-driven techniques.

To describe the CDA algorithm, suppose $\mathbf{u}(t)$ is a solution of a dissipative dynamical system governed by

$$(1.3) \quad \frac{d\mathbf{u}}{dt} = F(\mathbf{u}),$$

where the initial data $\mathbf{u}(0) = \mathbf{u}_0$ is not fully known. We denote the observable state of the solution by $I_h(\mathbf{u})$, where I_h is an autonomous, bounded linear operator representing an orthogonal projection onto a finite-dimensional subspace of $L^2(\Omega)$. This operator satisfies

the approximation property

$$(1.4) \quad \|\phi - I_h(\phi)\|_{L^2(\Omega)} \leq C_1 h \|\nabla \phi\|_{L^2(\Omega)},$$

for all $\phi \in H^1(\Omega)$, where $C_1 > 0$ is a constant independent of the discretization parameter h . The operator I_h approximates the true state by utilizing only the information available from global coarse spatial observations h . In the context of incompressible flows considered in this work, I_h is understood to first interpolate the observed data, and then apply an orthogonal projection onto the space of divergence-free (solenoidal) vector fields. Consequently, I_h is idempotent and self-adjoint, i.e., $I_h^2 = I_h$ and $I_h^* = I_h$. Examples include the orthogonal projection onto low Fourier modes [41] and, as a more physically motivated example, interpolation using piecewise polynomial finite element spaces [39].

Using the CDA algorithm introduced in [3], the observations $I_h(\mathbf{u}(t))$ are incorporated into an auxiliary system given by

$$(1.5) \quad \frac{d\mathbf{v}}{dt} = F(\mathbf{v}) + \mu (I_h(\mathbf{u}) - I_h(\mathbf{v})),$$

with an *arbitrary* initial condition \mathbf{v}_0 . Under appropriate conditions, that is, sufficiently large μ and sufficiently small h , one can have

$$\mathbf{v}(t) \rightarrow \mathbf{u}(t)$$

exponentially fast in a suitable function space.

Interpolation-based nudging has been extensively studied from both theoretical and computational perspectives. Foundational theoretical results include the convergence and error analysis for the 2D NSE by Azouani, Olson, and Titi [3], later extended to the 3D setting by Biswas and Price [7]. Additional error estimates using the L^2 projection operator were developed by Rebholz and Zerfas [54]. Interpolation-based nudging has a wide application to diverse fluid dynamics problems, as seen in [1, 4, 11, 18, 20, 21, 23, 24, 31, 32, 38, 40, 51, 52, 60]. Beyond idealized models, recent research has demonstrated that data assimilation via interpolant nudging remains effective even with model errors or noisy observations [15, 33, 45, 60]. The selection of the nudging parameter μ , which controls assimilation strength, has been shown to be critical for performance, and several works have proposed adaptive or optimized selection methods [17, 61]. Alternative data assimilation frameworks such as ensemble Kalman filters and 3D/4D-VAR methods [8, 43], but interpolation-based nudging remains attractive for its simplicity and provable convergence properties.

Organization of this paper. In Section 2, we introduce the inequalities and preliminary results on the NSE used in our analysis. Section 3 provides a brief background on the finite element method and the numerical schemes used throughout our simulations; more importantly, we detail how the global Direct Numerical Simulation (DNS) mesh is constructed

from the coarse local observational mesh. In Section 4, we state and prove our main theoretical results. The three numerical experiments, each demonstrating and extending beyond the analytical results, are described in Sections 5, 6, and 7. Finally, in Section 8, we discuss potential improvements and future directions.

2. PRELIMINARIES

The results in this section are standard and can be found in any classical text on the NSE [26] or functional analysis [9].

Let $\mathbf{x} = (x_1, x_2) \in \mathbb{R}^2$ and $\Omega \subset \mathbb{R}^2$ be a bounded domain with C^2 boundary. Let $1 \leq p \leq \infty$, and denote by p' the conjugate exponent defined by $\frac{1}{p} + \frac{1}{p'} = 1$. Assume that $\phi \in L^p(\Omega)$ and $\psi \in L^{p'}(\Omega)$. Then Hölder's inequality states that

$$(2.1) \quad \|\phi \psi\|_{L^1(\Omega)} \leq \|\phi\|_{L^p(\Omega)} \|\psi\|_{L^{p'}(\Omega)}.$$

Additionally, for any $a, b \geq 0$ and $\lambda > 0$, Young's inequality takes the form

$$(2.2) \quad ab \leq \lambda a^p + \frac{1}{p'} (p\lambda)^{-\frac{p'}{p}} b^{p'}.$$

For any $\phi \in H^1(\Omega)$, Ladyzhenskaya's inequality states

$$(2.3) \quad \|\phi\|_{L^4(\Omega)} \leq 2^{1/4} \|\phi\|_{L^2(\Omega)}^{1/2} \|\nabla \phi\|_{L^2(\Omega)}^{1/2}.$$

Let $d(\mathbf{x}) = \text{dist}(\mathbf{x}, \partial\Omega)$. Then, for any $\mathbf{u} \in W_0^{1,p}(\Omega)$, Hardy's inequality states that there exists a dimensionless constant C_p such that

$$(2.4) \quad \left\| \frac{\mathbf{u}}{d} \right\|_{L^p(\Omega)} \leq C_p \|\nabla \mathbf{u}\|_{L^p(\Omega)}.$$

To support the forthcoming analysis, we first recall some fundamental results of (1.1). These results are well-known and documented in the literature (see, for example, [26, 57]). Denote by λ_1 the smallest eigenvalue of the Stokes operator, then for $\phi \in H^1$, the Poincaré's inequality reads as

$$(2.5) \quad \lambda_1 \|\phi\|^2 \leq \|\nabla \phi\|^2.$$

A key non-dimensional parameter that captures the complexity of the system is the Grashof number, given by

$$(2.6) \quad G := \frac{1}{\nu^2 \lambda_1} \|\mathbf{f}\|_{L^2(\Omega)}.$$

Theorem 2.1 (Existence and Uniqueness of Strong Solutions in 2D). *Suppose $\mathbf{u}_0 \in H^1(\Omega)$ and $\mathbf{f} \in L^\infty((0, \infty); L^2(\Omega))$. Then, for any $T > 0$, the initial value problem (1.1) admits a unique strong solution \mathbf{u} satisfying*

$$\mathbf{u} \in C([0, T]; L^2(\Omega)) \cap L^2(0, T; H^1(\Omega)), \quad \partial_t \mathbf{u} \in L^2(0, T; L^2(\Omega)).$$

Theorem 2.2. *Fix $T > 0$, and let G be the Grashof number as defined in (2.6). Suppose that \mathbf{u} is the solution of (1.1) corresponding to the initial value \mathbf{u}_0 . Then, there exists a time t_0 , depending on \mathbf{u}_0 , such that for all $t \geq t_0$, we have:*

$$\|\mathbf{u}(t)\|^2 \leq 2\nu^2 G^2,$$

and

$$\int_t^{t+T} \|\nabla \mathbf{u}(\tau)\|^2 d\tau \leq 2(1 + T\nu\lambda_1)\nu G^2.$$

Proposition 2.3 (Uniform Gronwall Inequality). *Let $T > 0$ be fixed. Suppose*

$$\frac{d}{dt}Y + \alpha(t)Y \leq 0,$$

where

$$\limsup_{t \rightarrow \infty} \int_t^{t+T} \alpha(s)ds \geq \alpha_0 > 0,$$

then $Y(t) \rightarrow 0$, exponentially, as $t \rightarrow \infty$.

3. MESH CONSTRUCTION AND NUMERICAL IMPLEMENTATION

In this section, we introduce the necessary notation for the finite element method and provide details on how the global mesh used for solving the full system is constructed from the coarse local observational mesh, an essential component of our approach.

Let $\Omega \subset \mathbb{R}^2$ be a bounded domain with C^2 boundary, and let $\Omega_0 \subset \Omega$ be a subdomain; see Figure 1a. We define δ to be the maximum distance between any point in Ω and the subdomain Ω_0 ; that is

$$\delta := \sup_{x \in \Omega} \text{dist}(x, \Omega_0).$$

From this point onward, we denote by Ω_δ the region between Ω and Ω_0 ; that is

$$\Omega_\delta := \Omega \setminus \overline{\Omega_0}.$$

Denote the natural function spaces for velocity and pressure, respectively, by

$$\begin{aligned} \mathbf{X} &:= \mathbf{H}_0^1(\Omega) = \{\mathbf{u} \in \mathbf{H}^1(\Omega) : \mathbf{u} = 0 \text{ on } \partial\Omega\}, \\ Q &:= L_0^2(\Omega) = \left\{q \in L^2(\Omega) : \int_{\Omega} q dx = 0\right\}, \\ \mathbf{V} &:= \{\mathbf{u} \in \mathbf{X} : (\nabla \cdot \mathbf{u}, q) = 0 \text{ for all } q \in Q\}. \end{aligned}$$

Denote by Ω_h a regular, conforming triangulation of the domain Ω , and let $\mathbf{X}^h \subset \mathbf{X}$ and $Q^h \subset Q$ be an inf-sup stable pair of discrete velocity-pressure spaces (see [37] for more details). Additionally, we define the discretely divergence-free space \mathbf{V}^h as

$$\mathbf{V}^h := \{\mathbf{v}^h \in \mathbf{X}^h : (q^h, \nabla \cdot \mathbf{v}^h) = 0 \text{ for all } q^h \in Q^h\}.$$

For all simulations, following Algorithm 3.1, we employ the IMEX (implicit-explicit) scheme for temporal discretization to avoid solving a nonlinear problem at each time step. The spatial discretization is based on the finite element method. We assume the velocity–pressure finite element spaces $(\mathbf{X}^h, Q^h) = (\mathbb{P}_2, \mathbb{P}_1)$, known as the Taylor–Hood elements, which satisfy the inf-sup stability condition, see [47] Chapter 9 for detailed description on the scheme.

Algorithm 3.1. Given body force $\mathbf{f} \in L^\infty((0, \infty), L^2(\Omega))$, initial condition $\mathbf{v}_0 \in \mathbf{V}^h$, reference solution \mathbf{u}_{n+1} , and $(\mathbf{v}_n^h, q_n^h) \in \mathbf{X}^h \times Q^h$, compute $(\mathbf{v}_{n+1}^h, q_{n+1}^h) \in \mathbf{X}^h \times Q^h$ satisfying

$$(3.1) \quad \begin{aligned} \left(\frac{\mathbf{v}_{n+1}^h - \mathbf{v}_n^h}{\Delta t}, \Theta^h \right) + b(\mathbf{v}_n^h, \mathbf{v}_{n+1}^h, \Theta^h) + \nu (\nabla \mathbf{v}_{n+1}^h, \nabla \Theta^h) - (q_{n+1}^h, \nabla \cdot \Theta^h) \\ = (\mathbf{f}_{n+1}, \Theta^h) - \mu (I_H(\mathbf{v}_{n+1}^h - \mathbf{u}_{n+1}), \Theta^h), \end{aligned}$$

$$(3.2) \quad (\nabla \cdot \mathbf{v}_{n+1}^h, r^h) = 0,$$

for all $(\Theta^h, r^h) \in \mathbf{X}^h \times Q^h$.

In order to minimize uncertainties, maintain full control over the resolution of observations, and assess the accuracy of the reconstruction, we extract the observations from an independent DNS. While $I_H(\mathbf{u}_{n+1})$ denotes the local observations restricted to the subdomain Ω_0 at a coarse spatial resolution and at time step t_{n+1} , the global approximating solution \mathbf{v}^h , initialized from an arbitrary initial condition, is computed using Algorithm 3.1. Note that at time t_{n+1} , the relevant data about the true solution have already been acquired; therefore, $I_H(\mathbf{u}_{n+1})$ is interpreted as the most recent data gathered locally throughout Ω_0 . In all experiments, the algorithms are implemented using the public domain finite element software **FreeFEM++** [34]. Throughout all our numerical tests, the precision and robustness of the reconstruction are assessed by comparing the locally assimilated solution \mathbf{v}^h , computed using the above algorithm, with the reference solution \mathbf{u}^h obtained from DNS.

Local-to-Global Mesh Construction. One challenge in our simulation lies in constructing a local coarse finite element mesh for the interpolation operator that is compatible with the global DNS mesh used to solve the whole system. This compatibility ensures mathematical consistency and numerical stability, while enabling localized data assimilation. Before presenting the main results, we demonstrate this process on a general two-dimensional domain. Consider a Bézier surface representing the bounded physical domain $\Omega \subset \mathbb{R}^2$, and let $\Omega_0 \subset \Omega$ denote the observation subdomain where local coarse spatial measurements are available; Figure 1a. We first construct the coarsest mesh of size H within Ω_0 , corresponding to the resolution at which local observational data are collected, see Figure 1b. Each coarse

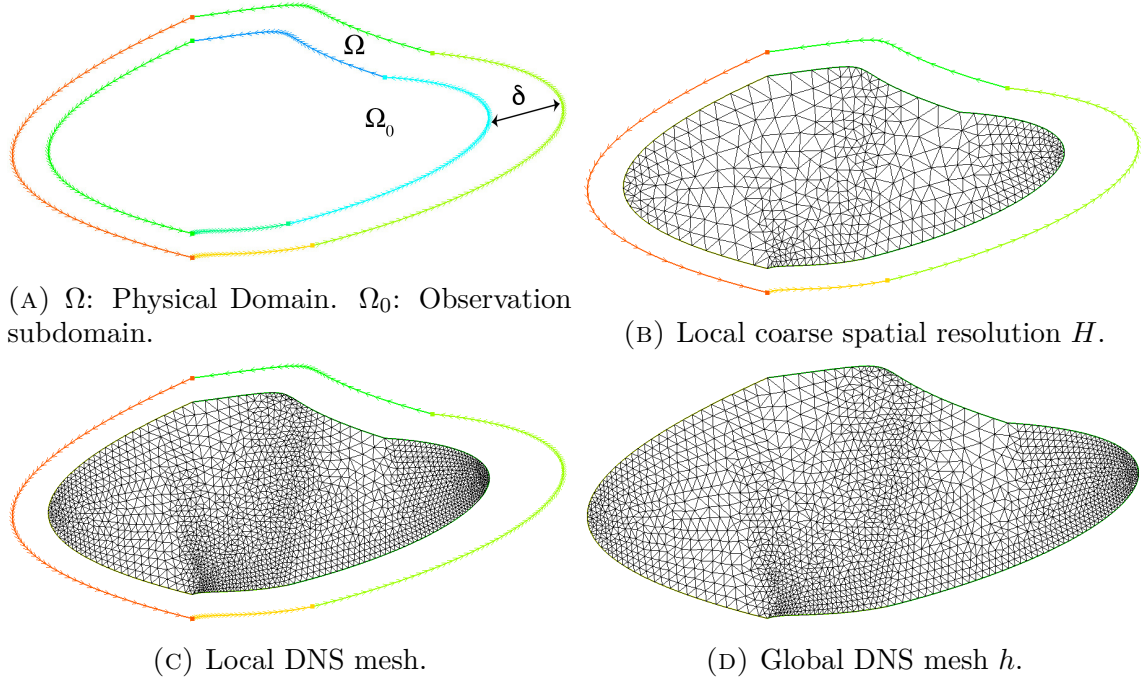


FIGURE 1. Domain mesh setup: from local coarse observations to global DNS mesh.

grid cell is then split into more sub-triangles to generate a fine mesh, consistent with the resolution of DNS, within the subdomain Ω_0 , see Figure 1c. Finally, this fine mesh is extended to cover the entire domain Ω , with h denoting the finest global DNS mesh size; Figure 1d.

4. RIGOROUS ANALYSIS; SYNCHRONIZATION

Theorem 4.1. *Let $\Omega \subset \mathbb{R}^2$ be a bounded domain with C^2 boundary, and let $\Omega_0 \subset \Omega$ be a subdomain with $\delta := \sup_{x \in \Omega} \text{dist}(x, \Omega_0)$. Let \mathbf{u} be a solution of the incompressible two-dimensional NSE (1.1) on Ω , equipped with no-slip Dirichlet boundary conditions. Let \mathbf{v} be the approximating solution given by (1.2), where I_H is the localization operator that incorporates observational data from the subregion Ω_0 , and satisfies (1.4). Then,*

$$\|\mathbf{u} - \mathbf{v}\|_{L^2(\Omega)} \rightarrow 0,$$

provided that the following conditions hold:

$$4C_1\mu H^2 \leq \nu, \quad \mu \geq 4G^2\nu\lambda_1, \quad \text{and} \quad \delta \leq \frac{C_1}{C_p} H.$$

Remark 4.2. The boundary layer condition can be relaxed throughout the practice/simulation. The above restrictions on the parameters μ , H , and particularly the condition $\delta \lesssim H \sim \mathcal{O}(\nu^{1/2})$, may appear overly conservative from a practical standpoint.

However, such limitations are well understood in the context of data assimilation and its rigorous analytical framework (see, for instance, [11, 12, 22, 30, 32, 39, 54, 61]), where the bounds arise from classical inequalities and energy estimates that are not easily sharpened, but are nonetheless standard and widely accepted. These theoretical restrictions are significantly relaxed in practice, as demonstrated throughout our simulations. Consequently, developing less restrictive analytical criteria, possibly through alternative mathematical techniques or problem-specific refinements, that better reflect the robustness observed in computational experiments remains an open and compelling direction for future research.

Proof. Subtracting (1.1) and (1.2), the difference $\mathbf{e} = \mathbf{u} - \mathbf{v}$ satisfies

$$\partial_t \mathbf{e} + \mathbf{e} \cdot \nabla \mathbf{u} + \mathbf{v} \cdot \nabla \mathbf{e} - \nu \Delta \mathbf{e} + \nabla(p - q) = -\mu I_H(\mathbf{e}), \quad \nabla \cdot \mathbf{e} = 0.$$

Using incompressibility, and after L^2 multiplication of the above difference equation with \mathbf{e} , we arrive at

$$(4.1) \quad \frac{1}{2} \frac{d}{dt} \|\mathbf{e}\|_{L^2(\Omega)}^2 + \nu \|\nabla \mathbf{e}\|_{L^2(\Omega)}^2 = -(\mathbf{e} \cdot \nabla \mathbf{u}, \mathbf{e}) - \mu \|I_H(\mathbf{e})\|_{L^2(\Omega_0)}^2 := \text{I} + \text{II}.$$

Using Hölder's and Young inequalities (2.1) and (2.2), along with (2.3), Term I in the above is estimated as

$$(4.2) \quad \begin{aligned} |(\mathbf{e} \cdot \nabla \mathbf{u}, \mathbf{e})| &\leq \|\mathbf{e}\|_{L^4(\Omega)}^2 \|\nabla \mathbf{u}\|_{L^2(\Omega)} \leq 2^{\frac{1}{2}} \|\mathbf{e}\|_{L^2(\Omega)} \|\nabla \mathbf{e}\|_{L^2(\Omega)} \|\nabla \mathbf{u}\|_{L^2(\Omega)} \\ &\leq \frac{\nu}{2} \|\nabla \mathbf{e}\|_{L^2(\Omega)}^2 + \frac{1}{\nu} \|\nabla \mathbf{u}\|_{L^2(\Omega)}^2 \|\mathbf{e}\|_{L^2(\Omega)}^2. \end{aligned}$$

Next we estimate term II in (4.1). First note that

$$(4.3) \quad \|\mathbf{e}\|_{L^2(\Omega)}^2 = \|\mathbf{e}\|_{L^2(\Omega_0)}^2 + \|\mathbf{e}\|_{L^2(\Omega_\delta)}^2 \leq \|I_H(\mathbf{e})\|_{L^2(\Omega_0)}^2 + \|(I - I_H)(\mathbf{e})\|_{L^2(\Omega_0)}^2 + \|\mathbf{e}\|_{L^2(\Omega_\delta)}^2,$$

The second term on the right-hand side of the above inequality can be bounded as follows

$$\|(I - I_H)(\mathbf{e})\|_{L^2(\Omega_0)}^2 \leq (C_1 H)^2 \|\nabla \mathbf{e}\|_{L^2(\Omega_0)}^2 \leq (C_1 H)^2 \|\nabla \mathbf{e}\|_{L^2(\Omega)}^2.$$

Then, using Hardy's inequality (2.4), we obtain the following estimate for the last term in (4.3)

$$\|\mathbf{e}\|_{L^2(\Omega_\delta)}^2 \leq (C_p \delta)^2 \|\nabla \mathbf{e}\|_{L^2(\Omega_\delta)}^2 \leq (C_p \delta)^2 \|\nabla \mathbf{e}\|_{L^2(\Omega)}^2.$$

Now from (4.3), and the above two estimates, one can obtain

$$(4.4) \quad \|I_H(\mathbf{e})\|_{L^2(\Omega_0)}^2 \geq \|\mathbf{e}\|_{L^2(\Omega)}^2 - 2 \max\{C_1^2 H^2, C_p^2 \delta^2\} \|\nabla \mathbf{e}\|_{L^2(\Omega)}^2.$$

With assumptions $\delta \leq \frac{C_1}{C_p} H$ and $4 C_1 \mu H^2 \leq \nu$, and using estimates (4.2) and (4.4) in (4.1), we get the following

$$\frac{d}{dt} \|\mathbf{e}\|_{L^2(\Omega)}^2 + \left[2\mu - \frac{1}{2\nu} \|\nabla \mathbf{u}\|_{L^2(\Omega)}^2 \right] \|\mathbf{e}\|_{L^2(\Omega)}^2 \leq 0.$$

Next, using the bounds established in Theorem 2.2, one can choose $T = \frac{1}{\nu\lambda_1}$ and $\mu \geq 4G^2\nu\lambda_1$ to obtain

$$\limsup_{t \rightarrow \infty} \int_t^{t+T} \left(2\mu - \frac{1}{2\nu} \|\nabla \mathbf{u}\|_{L^2(\Omega)}^2 \right) ds \geq \alpha_0 =: 2G^2 > 0.$$

Then, applying the standard Gronwall inequality (Proposition 2.3) with

$$\alpha(t) = 2\mu - \frac{1}{2\nu} \|\nabla \mathbf{u}\|_{L^2(\Omega)}^2,$$

it follows that $\|\mathbf{e}\|_{L^2(\Omega)}^2 \rightarrow 0$ exponentially as $t \rightarrow \infty$. \square

Remark 4.3. We note that, under higher regularity assumptions such as $\nabla u \in L^\infty(\Omega)$, as considered by García-Archilla, Novo, and Titi [29], there may be potential to improve the upper bound on the nudging parameter μ . A detailed investigation of this possibility is left to the interested reader.

5. COMPUTATIONAL STUDY I: FLOW OVER A FLAT OBSTACLE

In this section, using Algorithm 3.1, we conduct a numerical test of flow over a flat obstacle, which is based on the setup described in [30, 61]. The computational domain is a rectangular channel, $[-7, 20] \times [0, 20]$, that contains a flat plate obstacle of size 0.125×1 , centered at $(0.075, 0)$. We study the effect of local DA by dividing the domain Ω into three sub-domains, $\Omega_j \subset \Omega$, $j = 1, 2, 3$ (Figure 2a), defined as follows:

- Region 1 (Ω_1): A box-shaped region centered around the flat plate, with $2l$ thickness extending beyond both the length and width of the plate.
- Region 2 (Ω_2): The region between the top and bottom wall layers and the box-shaped region.
- Region 3 (Ω_3): The boundary layers with thickness l near the top and bottom walls.

With the above setup, we examine three cases. First, for thickness parameter $l = 1$, we generate a coarse mesh of resolution H on each subdomain using Delaunay–Voronoi triangulation methods (see Figure 2a), where the observational data are collected. Each triangle in this coarse mesh is then subdivided to create a finer DNS mesh of resolution h ; see Table 1 for detailed information about this configuration. In addition, to vary the data density and the number of observational data points, we adjust the observed regions $\Omega_1, \Omega_2, \Omega_3$ by increasing the layer thickness to $l = 2$ and $l = 3$ (see Figures 2b and 2c). In each configuration, Regions 1 and 3 expand, while Region 2 shrinks accordingly. See Tables 2 and 3 for further details.

We do not impose an external force, and the flow is driven by the inflow velocity, $u_{\text{in}} = (1, 0)^T$. We impose the no-slip boundary conditions at the obstacle and walls, and a weak zero-traction boundary condition at the outflow. We set the Reynolds number $\mathcal{R}e \sim 600$, a time step of $\Delta t = 0.02$, and a final time of $T = 81$, corresponding to three turnover

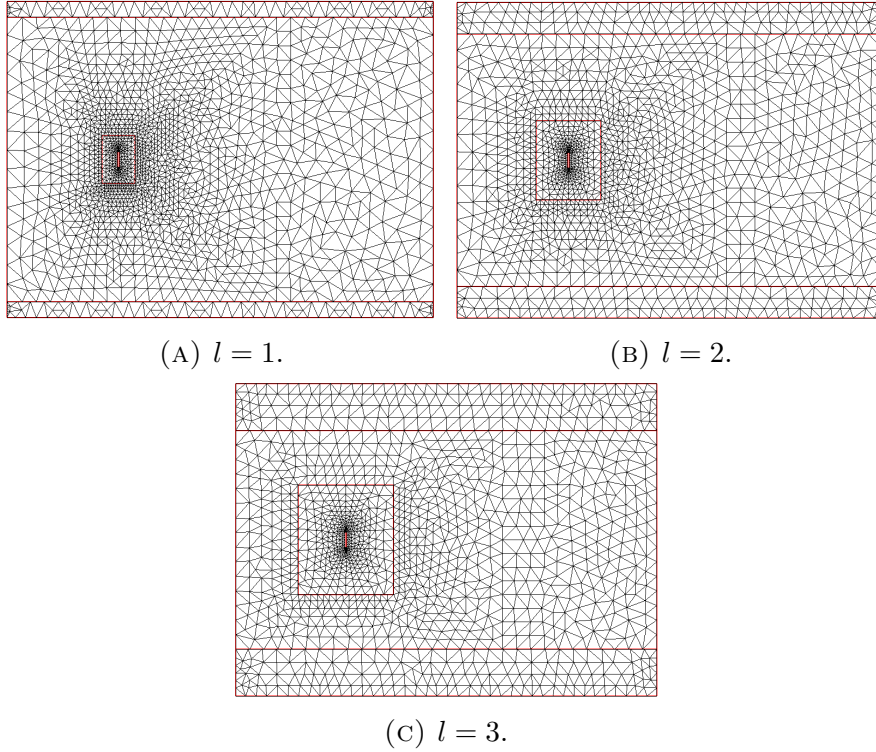


FIGURE 2. Local coarse mesh construction within the domain Ω , showing three sub-domains. Region 1 (Ω_1): a box-shaped region centered around the flat plate, Region 2 (Ω_2): the interior region between the top and bottom wall layers and the box-shaped region. And Region 3 (Ω_3): the boundary layers near the top and bottom walls.

Domain	# Vertices	# Vertices per Area	Max size of mesh
Ω (DNS)	7322	14	0.85
Ω_1	278	45	0.40
Ω_2	1447	3	1.70
Ω_3	204	4	1.16

TABLE 1. Details on the flow over a flat obstacle meshes for $l = 1$.

times. Here, the turnover time is based on the full streamwise domain length, long wall length = 27. Since this test examines a through-flow problem, it evaluates errors over three turnover times rather than an extended period. Nevertheless, the flow is complex, with many intriguing features, and is a standard test problem [30, 61].

Domain	# Vertices	# Vertices per Area	Max size of mesh
Ω (DNS)	6312	12	0.75
Ω_1	364	18	0.68
Ω_2	1003	2	1.51
Ω_3	310	3	1.22

TABLE 2. Details on the flow over a flat obstacle meshes for $l = 2$.

Domain	# Vertices	# Vertices per Area	Max size of mesh
Ω (DNS)	5736	11	0.69
Ω_1	428	10	0.95
Ω_2	722	2	1.38
Ω_3	383	2	1.35

TABLE 3. Details on the flow over a flat obstacle meshes for $l = 3$.

The true initial condition \mathbf{u}_0 is generated by solving the steady Stokes problem with the same boundary conditions and zero external force, and then the true solution is generated by solving the NSE on the DNS global mesh h . The total degrees of freedom for the global fine mesh 50182. To initiate the data assimilation simulation, we assume that the flow in the DA system is initially at rest, i.e., $\mathbf{v}_0 = 0$ at $t = 0$, and we set the nudging parameter to $\mu = 5$.

Impact of Observation Placement: Boundary vs. Interior. Figure 3 shows the time evolution of the relative error in the L^2 norm of the velocity difference between the reference solution \mathbf{u} and the locally nudged solutions \mathbf{v} , with observational data collected from different regions: Region 1 (Ω_1), Region 2 (Ω_2), Region 3 (Ω_3), and the union of Regions 1 and 3 ($\Omega_1 \cup \Omega_3$). For comparison, the results of global (full-domain) nudging are also shown in each case (solid blue curve), where data are collected throughout the entire domain Ω . Across all three cases ($l = 1, 2, 3$), full synchronization is achieved when using data from the interior region Ω_2 , which is located away from the boundaries, though the convergence occurs slightly more slowly than in the global data assimilation case. In contrast, data collected near the boundaries (i.e., from Regions Ω_1 and Ω_3) contribute little to no improvement in synchronization. This limited effectiveness persists even when observations from Regions 1 and 3 are combined. Note that in our final simulation (Figure 3c), where the interior observation

region Ω_2 was reduced, global synchronization was still achieved. However, the convergence required considerably more time, underscoring that while interior observations are indeed sufficient, the spatial extent of the observed region plays a pivotal role in determining the efficiency of the assimilation process.

In addition, in Figure 4, we compare the performance of the local nudging algorithm focusing on Region 2, for different values of the layer thickness parameter l , over a longer time interval $T = 182$. The error corresponding to $l = 1$ decreases the fastest, reaching a full synchronization around $t = 15$. For $l = 2$, convergence occurs around $t = 60$, and for $l = 3$, the full synchronization is achieved near $t = 140$. This trend is due to the fact that expanding the observational region provides more information, which improves the assimilation performance.

5.1. Local DA with different nudging parameter. We also vary the nudging parameter μ applied to Region 2, with $\mu = 0, 1, 5, 10$ to study its effect on the error. We set $l = 1$ for all experiments. In Figures 5, we observe that DA applied to Region 2 shows significantly better results for larger μ , with $\mu = 5$ and $\mu = 10$ achieving similar results, over a longer period. For $\mu = 1$, a smaller value, the performance is much better than the no-DA system.

6. COMPUTATIONAL STUDY II: THE COUETTE FLOW

In this section, we examine two-dimensional Couette flow with tangential boundary conditions in the absence of a body force. Our numerical experiment is inspired by the work of Couette and Taylor, known as the Taylor experiment [28]. In Taylor's experiments, two concentric, very long cylinders are used, with the space between them filled with a liquid. Each cylinder can rotate independently. Consider a 2D slice of this experiment, where the domain Ω is an annulus defined as

$$\Omega = \{(x, y) \in \mathbb{R}^2 : 0.1^2 \leq x^2 + y^2 \leq 1^2\}.$$

The flow is driven by rotating both the inner and outer circles, with one rotating clockwise and the other counterclockwise. In the absence of a body force $\mathbf{f} = \mathbf{0}$, we consider the Reynolds number to be $\mathcal{R}e = 600$.

Within the domain Ω above, we introduce three sub-domains using artificial boundaries defined by the following parametric equations for $s \in [0, 2\pi]$ with

$$r_1 = 0.2 \text{ and } r_2 = 0.9$$

as

$$\begin{aligned} \text{Border } C_1(s) &: \{x = 0.1 \cos(s), y = 0.1 \sin(s)\}, \\ \text{Border } C_2(s) &: \{x = r_1 \cos(s), y = r_1 \sin(s)\}, \end{aligned}$$

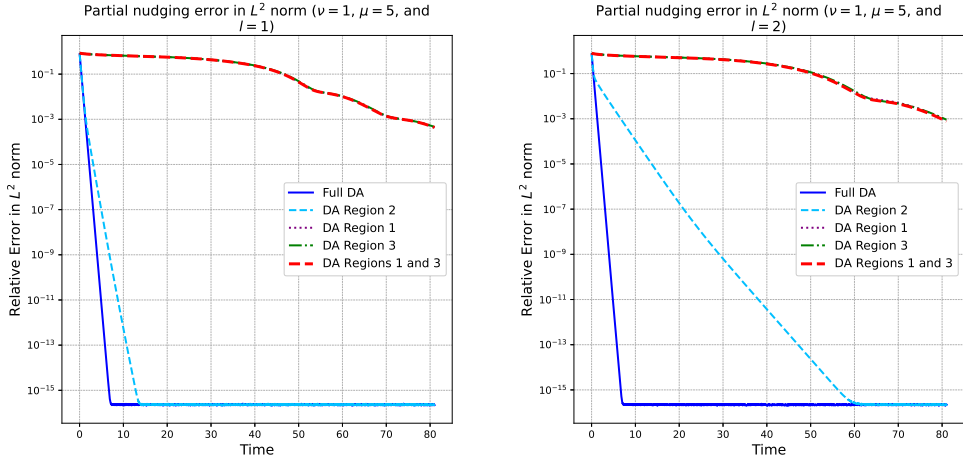
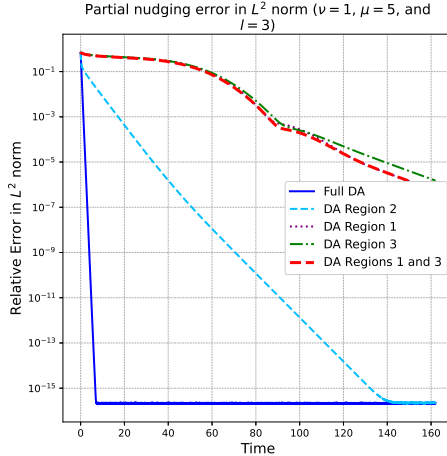
(A) Flow over a flat obstacle with $l = 1$. (B) Flow over a flat obstacle with $l = 2$.(C) Flow over a flat obstacle with $l = 3$.

FIGURE 3. Comparison of results using the local data assimilation algorithm applied to the flow over a flat obstacle with data collected from different regions of the domain: Ω_1 , Ω_2 , and Ω_3 .

$$\text{Border } C_3(s) : \{x = r_2 \cos(s), y = r_2 \sin(s)\},$$

$$\text{Border } C_4(s) : \{x = \cos(s), y = \sin(s)\}.$$

Using these boundaries, we define the three sub-domains, $\Omega_j \subset \Omega, j = 1, 2, 3$ (Figure 6), as follows

- Region 1 (Ω_1): The region enclosed between C_1 and C_2 , which is the area closest to the inner disc.

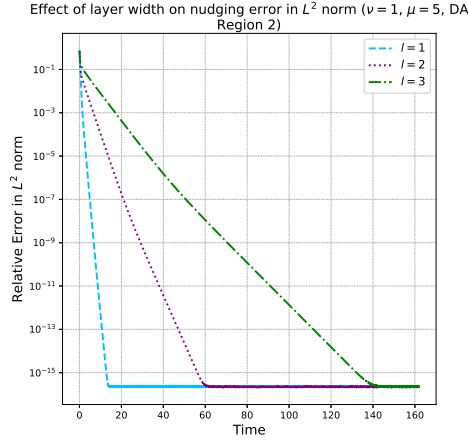


FIGURE 4. Relative error when applying local DA to Ω_2 with different l .

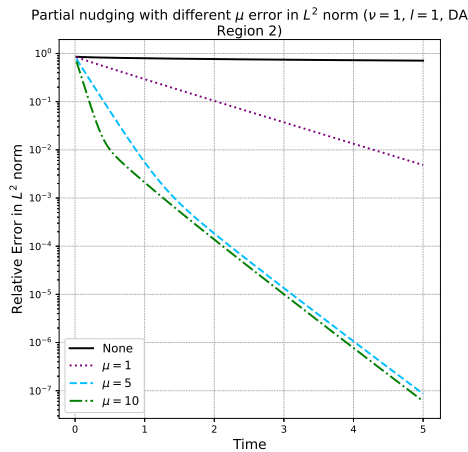


FIGURE 5. Relative error when applying DA to Ω with different μ values.

- Region 1 (Ω_2): The region enclosed between C_2 and C_3 , representing the area between the inner and outer regions.
- Region 1 (Ω_3): The region enclosed between C_3 and C_4 , which is the area closest to the outer boundary.

We first construct a coarse mesh H on each sub-domain using Delaunay-Voronoi methods, see Figure 6a, where the data are collected. Each triangular mesh is then split into four sub-meshes to generate the DNS mesh h . Throughout these refinements, we ensure that scales are resolved down to the Kolmogorov dissipation scale, $h_{\max} \leq \mathcal{R}e^{-\frac{1}{2}}$. Detailed information about both the DNS mesh and the local meshes can be found in Table 4.

Using the schemes described in Algorithm 3.1, we consider the time interval $[0, 100]$ with a time-step size $\Delta t = 0.01$, following the approach in [36]. To generate the initial condition

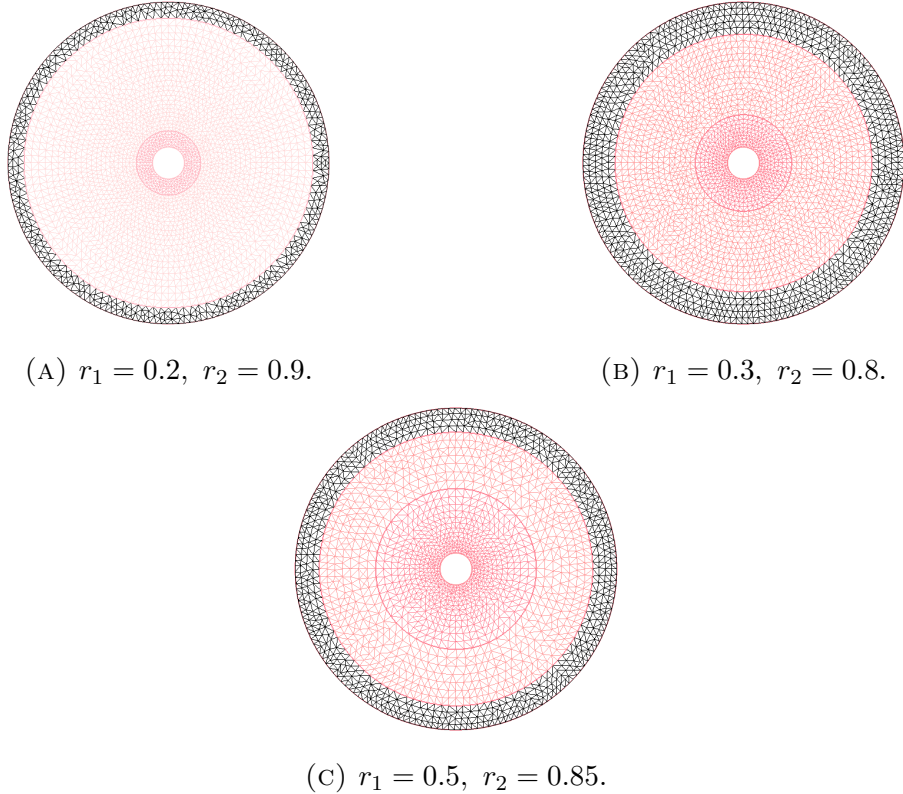


FIGURE 6. Local coarse mesh construction within the domain Ω showing three sub-domains: Ω_1 (closest to the inner disc - dark red), Ω_2 (between the inner and outer regions - light red), and Ω_3 (closest to the outer boundary - black).

Domain	# Vertices	# Vertices per Area	Max size of mesh
Ω (DNS)	12293	3965	0.037
Ω_1	356	3747	0.029
Ω_2	2379	992	0.064
Ω_3	572	969	0.074

TABLE 4. Details on the Couette spatial meshes for $r_1 = 0.2, r_2 = 0.9$.

for the true solution, we begin by running the simulation with the specified shear boundary condition from an initial state of zero up to $t = 5$. The resulting state at $t = 5$ is then used as the initial condition for subsequent simulations, denoted as \mathbf{u}_0^h . For the DA algorithms, we start from $\mathbf{v}_0^h = \mathbf{0}$ with $\mu = 10$. For the interpolant, we use local linear interpolation on a mesh H within the local region Ω_2 , which is four levels coarser than the DNS mesh.

Domain	# Vertices	# Vertices per Area	Max size of mesh
Ω (DNS)	10545	3401	0.032
Ω_1	526	2140	0.043
Ω_2	1425	828	0.057
Ω_3	919	813	0.064

TABLE 5. Details on the Couette spatial meshes for $r_1 = 0.3$, $r_2 = 0.8$.

Domain	# Vertices	# Vertices per Area	Max size of mesh
Ω (DNS)	7973	2571	0.042
Ω_1	747	996	0.071
Ω_2	733	495	0.084
Ω_3	747	858	0.066

TABLE 6. Details on the Couette spatial meshes for $r_1 = 0.5$, $r_2 = 0.85$.

Impact of Observation Placement: Boundary vs. Interior. Figure 7a shows the time evolution of the L^2 norm of the difference in velocities between the reference solution and the nudged solutions, using both local and global data assimilation. Full synchronization is achieved when data is used from the interior region Ω_2 , which lies away from the boundaries, although at a slightly slower rate compared to full-domain assimilation. In contrast, observational data collected near the boundaries (from regions Ω_1 and Ω_3) are found to be largely uninformative.

Next, we vary the regions of observed data two more times by adjusting the radius of the artificial boundaries $C_1(s)$ and $C_2(s)$ to

$$r_1 = 0.3 \quad \text{and} \quad r_2 = 0.8,$$

and

$$r_1 = 0.5 \quad \text{and} \quad r_2 = 0.85.$$

In these configurations, the outer subdomains Ω_1 and Ω_3 become larger, while the interior subdomain Ω_2 becomes smaller; see Figure 6b and Figure 6c. Detailed information about the DNS mesh and the local assimilation meshes is provided in Tables 5 and 6, respectively. The same phenomenon is observed (See Figures 7b and 7c): Full synchronization is consistently achieved when using data from the interior region Ω_2 , whereas data collected near the

boundaries (from regions Ω_1 and Ω_3) continue to have minimal to no impact on the assimilation process. In the final test 7c, where the interior observation region Ω_2 was considerably smaller, synchronization was still achieved, but only after a substantially longer simulation time. This further illustrates that while interior observations are sufficient, as expected, the size and density of the observational region strongly influence the rate of convergence.

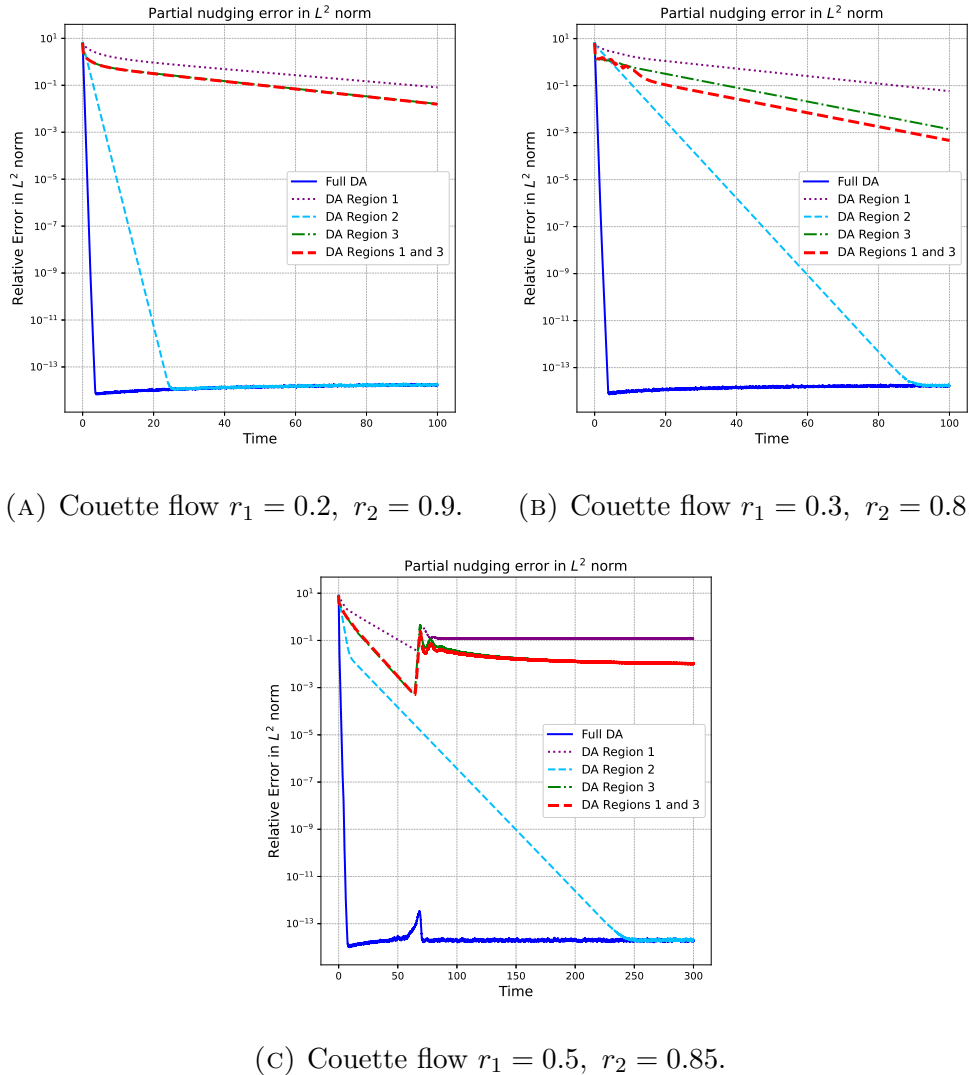


FIGURE 7. Comparison of results using the data assimilation algorithm applied to the 2D Couette flow with data collected from different regions of the domain: Ω_1 , Ω_2 , and Ω_3 .

7. COMPUTATIONAL STUDY III: FORCED FLOW WITH NON-HOMOGENEOUS DIRICHLET BOUNDARY CONDITIONS

For our third experiment, we consider the flow between offset circles. In short, comparing to the previous test in Section 6, we disrupt the symmetry of the domain and introduce a driven force. The domain consists of a disk with an inner smaller off-center disc removed, defined as

$$\Omega = \{(x, y) \in \mathbb{R}^2 : x^2 + y^2 \leq 1^2 \text{ and } (x - 0.2)^2 + y^2 \geq (0.1)^2\},$$

with no-slip boundary conditions on both circles. While the Reynolds number is $\mathcal{R}e = 600$, the flow is also driven by a counterclockwise rotational, time-independent body force

$$\mathbf{f}(x, y) = (-4y(1 - x^2 - y^2), 4x(1 - x^2 - y^2))^\top.$$

As the counterclockwise force applies, the flow rotates around $(0, 0)$ and interacts with the immersed circle (obstacle). This induces a von Kármán vortex street which interacts with the near wall streaks common in turbulent flow and a central vortex.

Using the same approach as before, each sub-domain Ω_1 , Ω_2 , and Ω_3 has been adjusted by shifting 0.2 units towards the x-axis, reflecting the relevant modifications, see Figure 8.

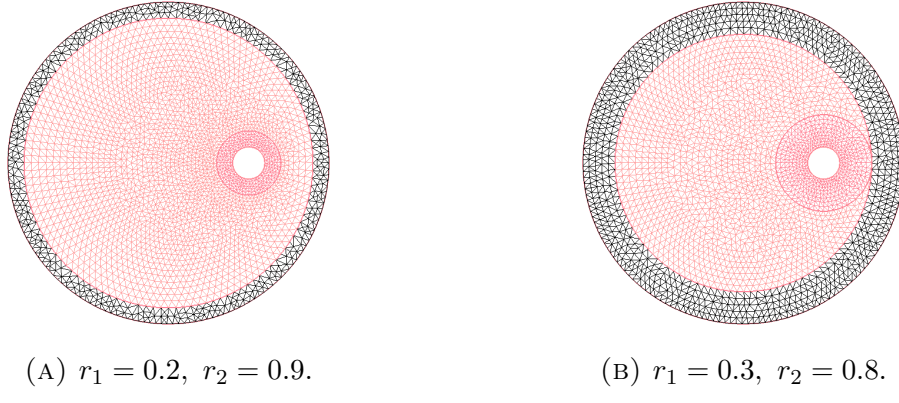
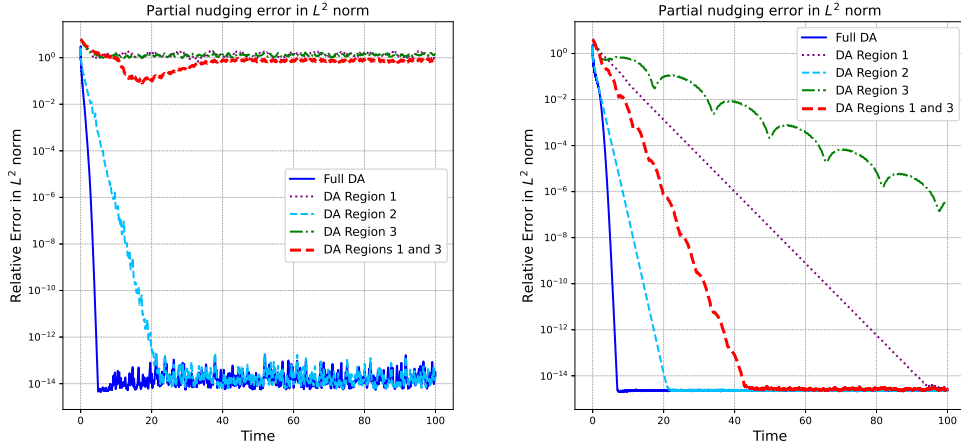


FIGURE 8. Local coarse mesh construction within the domain Ω showing three sub-domains: Ω_1 (closest to the inner disc - dark red), Ω_2 (between the inner and outer regions - light red), and Ω_3 (closest to the outer boundary - black).

The true initial condition \mathbf{u}_0 is generated by solving the steady Stokes problem with the same body forces $\mathbf{f}(x, y)$ and non-homogeneous boundary conditions. Given the absence of an exact solution for this problem, we adopt the DNS solution \mathbf{u}^h as our reference solution.

Impact of Observation Placement: Boundary vs. Interior. The results from this experiment (see Figures 9a and 9b) reaffirm the previous findings: assimilation using local data from the interior region Ω_2 , away from the boundaries, leads to global synchronization

up to the machine precision, while observations taken near the boundary regions Ω_1 and Ω_3 provide little to no useful information for the assimilation process.



(A) Flow between offset circles $r_1 = 0.2$, $r_2 = 0.9$. (B) Flow between offset circles $r_1 = 0.3$, $r_2 = 0.8$.

FIGURE 9. Comparison of results using the DA algorithm applied to the forced flow between offset circles with data collected from different regions of the domain: Ω_1 , Ω_2 , and Ω_3 .

8. DISCUSSION

Given the chaotic nature of turbulent flow, estimating the turbulent state by simply interpolating sparse observations is ineffective. DA addresses this challenge by combining observations (collected through sensors or other measurement techniques) with numerical simulations based on the governing physical model, thereby enabling high-fidelity reconstruction of the entire flow state. Due to practical limitations in sensor placement, efficiently reconstructing the full turbulent flow requires strategic positioning of sensors, targeting flow features that most strongly influence the system; so that each observation provides maximal information about the overall dynamics. This challenge is addressed in the present work using the nudging algorithm. This work highlights the potential of localized DA to reduce observational costs while maintaining predictive fidelity.

Previous studies employing a range of methodologies [5, 19, 56, 58] have shown that wall data can be used to reconstruct near-wall turbulence and, beyond that, only the outer large-scale structures of the flow. Our results resonate with the findings of Zaki and Wang [59], who observed that while wall measurements can reveal near-wall turbulent structures, only the large-scale motions in the outer flow are recoverable from such data. Beyond this, our simulations confirm that observations collected near the boundary are insufficient to reconstruct

the full flow field with high fidelity. However, in contrast to the limitations of wall-based sensing, we demonstrate, both theoretically and through numerical experiments, that it is possible to reconstruct the entire turbulent state, including small-scale structures, by utilizing interior observations located deeper within the bulk of the domain. This suggests that targeted sensing away from boundaries can offer greater predictive power than traditional wall-based approaches, highlighting the potential of strategically placed interior sensors for efficient flow reconstruction in practical settings.

In agreement with Biswas, Bradshaw, and Jolly [6], we also establish that full flow reconstruction is achievable using observations restricted to a subregion of the domain. While their theoretical results rely on spectral methods on a periodic 2D torus, our work extends these insights to a more physically realistic setting: the two-dimensional incompressible NSE on bounded domains with Dirichlet boundary conditions, with simulations performed using finite element methods over complex geometries. Notably, we observe that data near the boundaries are often uninformative.

One notable aspect of our findings is the limited utility of near-boundary observations in achieving global synchronization of the flow. While this may seem counterintuitive at first glance, it is consistent with insights from classical boundary layer theory, which suggest that near-wall dynamics are largely determined by viscosity and boundary conditions. According to Prandtl's theory, in the high Reynolds number regime, the effects of viscosity are confined to a thin region adjacent to the boundary (known as the boundary layer) whose thickness scales like $\delta_{BL} \sim \nu^{1/2}$ [53, 55]. Within this layer, the velocity field undergoes rapid transition to satisfy the no-slip Dirichlet condition, but its structure is highly constrained: it is slaved to the outer inviscid flow and strongly governed by the viscosity and imposed boundary conditions. Under standard assumptions, such as smooth geometry, regular data, and absence of flow separation, the behavior of the boundary layer is predictable and exhibits a universal profile that depends primarily on the external flow rather than on additional localized perturbations. Consequently, in such regimes, the near-wall dynamics contains limited information; once the viscosity and boundary data are fixed, the wall behavior is essentially determined.

Our theoretical and numerical results align closely with this perspective: we prove that global recovery is possible as long as the observational subregion lies within a distance $\mathcal{O}(\nu^{1/2})$ from all points in the domain, and in practice we observe robust synchronization even when this condition is exceeded. This threshold mirrors the classical boundary layer thickness, suggesting that the domain outside the layer, where the flow is more turbulent and less constrained, is where uncertainty is concentrated and observations are most valuable. Hence, the success of interior-only nudging can be interpreted as a manifestation of the physical structure of viscous flow: the boundary layer requires no direct correction, because its dynamics are determined indirectly through its coupling with the interior. In this way, our findings

not only extend the applicability of continuous data assimilation methods but also reveal a deep and previously unexplored connection between observability in dissipative systems and the classical structure of near-wall flow in fluid dynamics.

An important direction for future research concerns the sharpness of the geometric threshold $\delta \lesssim \nu^{1/2}$ established in our analysis. While our simulations suggest that synchronization can occur even when this bound is exceeded, it remains an open question whether the $\nu^{1/2}$ scaling is truly optimal or merely an artifact of the analytical methods employed. Constructing counterexamples in which synchronization provably fails for $\delta \gg \nu^{1/2}$ would help clarify this issue and further solidify the connection to Prandtl boundary layer theory, where $\nu^{1/2}$ governs the wall-layer thickness. Another promising avenue is the development of adaptive strategies for selecting the observational region Ω_0 . Instead of fixing this region a priori, it may be more efficient to place sensors based on dynamically evolving flow features, such as enstrophy, vorticity magnitude, or coherent structures like vortices (see, for example, the work of Franz, Larios, and Victor [27]). Finally, while our theoretical and computational results are restricted to two-dimensional flows, extending the local DA framework to three-dimensional turbulence presents both mathematical and numerical challenges. In particular, it is unclear whether interior-only nudging remains sufficient for achieving global synchronization in the presence of richer small-scale interactions and more complex boundary layer dynamics.

ACKNOWLEDGMENT

AP was partially supported by NSF grant DMS-2532987. RF was partially supported by NSF grant DMS-2410893.

REFERENCES

- [1] D. Albanez, H. N. Lopes, and E. Titi, *Continuous data assimilation for the three-dimensional Navier-Stokes- α* , Asymptotic Anal. **97** (2016), no. 1–2, 139–164.
- [2] M. Asch, M. Bocquet, and M. Nodet, *Data assimilation*, Fundamentals of Algorithms, vol. 11, SIAM, Philadelphia, PA, 2016. Methods, algorithms, and applications.
- [3] A. Azouani, E. Olson, and E. S. Titi, *Continuous data assimilation using general interpolant observables*, J. Nonlinear Sci. **24** (2014), no. 2, 277–304.
- [4] H. Bessaia, E. Olson, and E. S. Titi, *Continuous data assimilation with stochastically noisy data*, Nonlinearity **28** (2015), no. 3, 729–753.
- [5] T. R. Bewley and B. Protas, *Skin friction and pressure: The “footprints” of turbulence*, Physica D: Nonlinear Phenomena **196** (2004), no. 1–2, 28–44.
- [6] A. Biswas, Z. Bradshaw, and M. S. Jolly, *Data assimilation for the navier–stokes equations using local observables*, SIAM Journal on Applied Dynamical Systems **20** (2021), no. 4, 2174–2203.
- [7] A. Biswas and R. Price, *Continuous data assimilation for the three-dimensional navier–stokes equations*, SIAM Journal on Mathematical Analysis **53** (2021), no. 6, 6697–6723.

- [8] D. Blömker, K. Law, A. M. Stuart, and K. C. Zygalakis, *Accuracy and stability of the continuous-time 3dvar filter for the navier–stokes equation*, Nonlinearity **26** (2013), no. 8, 2193–2219.
- [9] H. Brezis, *Functional analysis, Sobolev spaces and partial differential equations*, Universitext, Springer, New York, 2011.
- [10] D. A. Buchta and T. A. Zaki, *Observation-infused simulations of high-speed boundary-layer transition*, Journal of Fluid Mechanics **916** (2021), A44, available at [2011.08265](#).
- [11] Y. Cao, A. Giorgini, M. Jolly, and A. Pakzad, *Continuous data assimilation for the 3D Ladyzhenskaya model: analysis and computations*, Nonlinear Analysis: Real World Applications **68** (2022), 103659.
- [12] Y. Cao, M. S. Jolly, E. S. Titi, and J. P. Whitehead, *Algebraic bounds on the rayleigh-bénard attractor*, Nonlinearity **34** (2021), no. 1, 509–531.
- [13] J. Charney, M. Halem, and R. Jastrow, *Use of incomplete historical data to infer the present state of the atmosphere*, J. Atmos. Sci. **26** (1969), 1160–1163.
- [14] J. Chen, M. Raiola, and S. Discetti, *An efficient offline sensor placement method for flow estimation*, Experimental Thermal and Fluid Science **167** (2025), 111448.
- [15] N. Chen, A. Farhat, and E. Lunasin, *Data assimilation with model error: Analytical and computational study for Sabra shell model*, Physica D: Nonlinear Phenomena **443** (2023), 133552.
- [16] R. Daley, *Atmospheric data analysis*, Cambridge Atmospheric and Space Science Series, Cambridge University Press, Cambridge, 1991.
- [17] A. E. Diegel, X. Li, and L. G. Rebholz, *Analysis of continuous data assimilation with large (or even infinite) nudging parameters*, Journal of Computational and Applied Mathematics **456** (2025), 116221.
- [18] A. E. Diegel and L. G. Rebholz, *Continuous data assimilation and long-time accuracy in a C^0 interior penalty method for the Cahn-Hilliard equation*, Applied Mathematics and Computation **424** (2022), 127042.
- [19] M. P. Encinar and J. Jiménez, *Logarithmic-layer turbulence: A view from the wall*, Physical Review Fluids **4** (2019), no. 11, 114603.
- [20] A. Farhat, N. E. Glatt-Holtz, V. R. Martinez, S. A. McQuarrie, and J. P. Whitehead, *Data assimilation in large prandtl rayleigh-bénard convection from thermal measurements*, SIAM J. Appl. Dyn. Syst. **19** (2020), no. 1, 510–540.
- [21] A. Farhat, M. Jolly, and E. S. Titi, *Continuous data assimilation for the 2d bénard convection through velocity measurements alone*, Phys. D **303** (2015), 59–66.
- [22] A. Farhat, A. Larios, V. R. Martinez, and J. P. Whitehead, *Identifying the body force from partial observations of a two-dimensional incompressible velocity field*, Physical Review Fluids **9** (2024), no. 5, 054602.
- [23] A. Farhat, E. Lunasin, and E. S. Titi, *Abridged continuous data assimilation for the 2d navier–stokes equations utilizing measurements of only one component of the velocity field*, J. Math. Fluid Mech. **18** (2016), no. 1, 1–23.
- [24] ———, *On the Charney conjecture of data assimilation employing temperature measurements alone: The paradigm of 3D planetary geostrophic model*, Math. Climate and Weather Forecast **2** (2016), 61–74.
- [25] C. Foias and G. Prodi, *Sur le comportement global des solutions non-stationnaires des équations de navier–stokes en dimension 2*, Rend. Sem. Mat. Univ. Padova **39** (1967), 1–34.
- [26] C. Foias, O. Manley, R. Rosa, and R. Temam, *Navier-Stokes equations and turbulence*, Encyclopedia of Mathematics and its Applications, vol. 83, Cambridge University Press, Cambridge, 2001.

- [27] T. Franz, A. Larios, and C. Victor, *The bleeps, the sweeps, and the creeps: Convergence rates for dynamic observer patterns via data assimilation for the 2d navier–stokes equations*, Computer Methods in Applied Mechanics and Engineering **392** (2022), 114673.
- [28] U. Frisch, *Turbulence: The legacy of a. n. kolmogorov*, Cambridge University Press, Cambridge, 1995.
- [29] Bosco García-Archilla, Julia Novo, and Edriss S. Titi, *Uniform in time error estimates for a finite element method applied to a downscaling data assimilation algorithm for the navier–stokes equations*, SIAM Journal on Numerical Analysis **58** (2020), no. 1, 410–429.
- [30] M. Gardner, A. Larios, L. G. Rebholz, D. Vargun, and C. Zerfas, *Continuous data assimilation applied to a velocity-vorticity formulation of the 2D navier–stokes equations*, Electronic Research Archive **29** (2021), no. 3, 2223–2247.
- [31] ———, *Continuous data assimilation applied to a velocity-vorticity formulation of the 2D Navier-Stokes equations*, American Institute of Mathematical Sciences Electronic Research Archive **29** (2021), no. 3, 2223–2247.
- [32] M. Gesho, E. Olson, and E. S. Titi, *A computational study of a data assimilation algorithm for the two-dimensional navier–stokes equations*, Commun. Comput. Phys. **19** (2016), no. 4, 1094–1110.
- [33] E. Hawkins, L. G. Rebholz, and D. Vargun, *Removing splitting/modeling error in projection/penalty methods for navier-stokes simulations with continuous data assimilation*, arXiv preprint arXiv:2302.05962 (2023).
- [34] F. Hecht, *New development in freefem++*, J. Numer. Math. **20** (2012), no. 3–4, 251–265.
- [35] J. E. Hoke and R. A. Anthes, *The initialization of numerical models by a dynamic-initialization technique*, Monthly Weather Review **104** (1976), no. 12, 1551–1556.
- [36] N. Jiang and W. Layton, *An algorithm for fast calculation of flow ensembles*, Int. J. Uncertain. Quantif. **4** (2014), no. 4, 273–301.
- [37] V. John, *Finite element methods for incompressible flow problems*, Springer Series in Computational Mathematics, vol. 51, Springer, Cham, 2016.
- [38] M. Jolly, V. R. Martinez, and E. S. Titi, *A data assimilation algorithm for the subcritical surface quasi-geostrophic equation*, Adv. Nonlinear Stud. **17** (2017), no. 1, 167–192.
- [39] M. Jolly and A. Pakzad, *Data assimilation with higher order finite element interpolants*, Internat. J. Numer. Methods Fluids **95** (2023), no. 3, 472–490.
- [40] M. S. Jolly, V. R. Martinez, E. J. Olson, and E. S. Titi, *Continuous data assimilation with blurred-in-time measurements of the surface quasi-geostrophic equation*, Chin. Ann. Math. Ser. B **40** (2019), no. 5, 721–764.
- [41] D. A. Jones and E. S. Titi, *Determining finite volume elements for the 2d navier–stokes equations*, Phys. D **60** (1992), no. 1–4, 165–174.
- [42] R. E. Kalman, *A new approach to linear filtering and prediction problems*, J. Basic Eng. **82** (1960), no. 1, 35–45.
- [43] E. Kalnay, *Atmospheric modeling, data assimilation, and predictability*, Cambridge Univ. Press, 2003.
- [44] R. E. Kistler, *A study of data assimilation techniques in an autobarotropic, primitive equation, channel model*, Ph.D. Thesis, 1974.
- [45] A. Larios and Y. Pei, *Approximate continuous data assimilation of the 2d navier–stokes equations via the voigt-regularization with observable data*, Evolution Equations and Control Theory **9** (2020), no. 3, 733–751.

- [46] K. Law, A. Stuart, and K. Zygalakis, *Data assimilation*, Texts in Applied Mathematics, vol. 62, Springer, Cham, 2015. A mathematical introduction.
- [47] W. Layton, *Introduction to the numerical analysis of incompressible viscous flows*, Computational Science & Engineering, vol. 6, SIAM, Philadelphia, PA, 2008.
- [48] E. N. Lorenz, *Deterministic nonperiodic flow*, Journal of Atmospheric Sciences **20** (1963), no. 2, 130–141.
- [49] ———, *The predictability of hydrodynamic flow*, Transactions of the New York Academy of Sciences **25** (1963), no. 4, 409–432.
- [50] ———, *A study of the predictability of a 28-variable atmospheric model*, Tellus **17** (1965), no. 3, 321–333.
- [51] J. Newey, J. P. Whitehead, and E. Carlson, *Model discovery on the fly using continuous data assimilation*, arXiv preprint arXiv:2411.13561 (2024).
- [52] Y. Pei, *Continuous data assimilation for the 3D primitive equations of the ocean*, Commun. Pure Appl. Anal. **18** (2019), no. 2, 643–661.
- [53] L. Prandtl, *Über flüssigkeitsbewegung bei sehr kleiner reibung*, Verhandlungen des dritten Internationalen Mathematiker-Kongresses **3** (1904), 484–491. Heidelberg. English translation in NACA TM 452 (1928).
- [54] L. G. Rebholz and C. Zerfas, *Simple and efficient continuous data assimilation of evolution equations via algebraic nudging*, Numerical Methods for Partial Differential Equations **37** (2021), no. 3, 2588–2612.
- [55] H. Schlichting and K. Gersten, *Boundary-layer theory*, 9th ed., Springer, Berlin, Heidelberg, 2017.
- [56] T. Suzuki and Y. Hasegawa, *Estimation of turbulent channel flow at $Re_\tau = 100$ based on the wall measurement using a simple sequential approach*, Journal of Fluid Mechanics **830** (2017), 760–786.
- [57] R. Temam, *Navier-Stokes equations. theory and numerical analysis*, Studies in Mathematics and its Applications, Vol. 2, North-Holland Publishing Co., Amsterdam-New York-Oxford, 1977.
- [58] M. Wang and T. A. Zaki, *State estimation in turbulent channel flow from limited observations*, Journal of Fluid Mechanics **917** (2021), A9.
- [59] T. A. Zaki and M. Wang, *From limited observations to the state of turbulence: Fundamental difficulties of flow reconstruction*, Physical Review Fluids **6** (2021), no. 10, 100501.
- [60] A. Çibik, R. Fang, W. Layton, and F. Siddiqua, *Data assimilation with model errors*, arXiv **2504.16291** (2025), available at [2504.16291](https://arxiv.org/abs/2504.16291).
- [61] A. Çibik, R. Fang, W. Layton, and F. Siddiqua, *Adaptive parameter selection in nudging based data assimilation*, Computer Methods in Applied Mechanics and Engineering **433** (2025), 117526.

(Fang) DEPARTMENT OF MATHEMATICS, THE OHIO STATE UNIVERSITY

Email address: fang.1211@osu.edu

(Pakzad) DEPARTMENT OF MATHEMATICS, CALIFORNIA STATE UNIVERSITY NORTHRIDGE

Email address: pakzad@csun.edu